Numerical and physical modeling of the effect of cone apex angle on the penetration resistance in coarse-grained soils

Hunt, O.M.[1], O'Hara, K.B.[2], Chen, Y.[3], and Martinez, A.[4]

[1]HDR engineering, 2379 Gateway Oaks Dr., Sacramento CA, 95833; email: olivia.hunt@hdrinc.com

[2]Department of Civil and Environmental Engineering, University of California Davis, 2001 Ghausi Hall, Davis CA, 95616; e-mail: kbohara@ucdavis.edu

[3]Department of Civil and Environmental Engineering, University of California Davis, 2001 Ghausi Hall, Davis CA, 95616; e-mail: yych@ucdavis.edu

[4]Department of Civil and Environmental Engineering, University of California Davis, 2001 Ghausi Hall, Davis CA, 95616; e-mail: amart@ucdavis.edu

Abstract

The tip shape of penetrometers and piles has an important influence on the soil resistance mobilized during penetration. Blunt or flat tips typically generate greater penetration resistances, which can lead to refusal during in-situ testing and pile driving in the field. Results are presented from numerical and experimental investigations on probes with conical tips of varying apex angles to quantify the effect of the apex angle on the mobilized penetration resistance and associated failure mechanisms. Discrete Element Modeling (DEM) simulations were performed in unconfined and confined (i.e., stress-controlled) specimens to model shallow and deep penetration conditions, respectively. Centrifuge penetration tests were performed by quasi-statically advancing an instrumented probe to a depth-to-probe-diameter ratio of 16.7. The numerical and experimental results indicate that at shallow depths, the sharper tips mobilize smaller penetration resistances. In deep penetration conditions, the changes in penetration resistance with tip apex angle are less pronounced. Based on the results of the two investigations and values reported in the literature, a relationship characterizing the functional form between tip apex angle and normalized penetration resistance is proposed. A meso-scale analysis of the DEM simulation shows differences in the failure mechanisms induced by sharp and blunt tips: the zone where large particle displacements and stress changes occur is large and located below the tip for penetration with blunt tips, whereas the zone is smaller and located both laterally and below the tip for sharp tips.

1. Introduction

It has been widely reported that the tip shape of penetrometers or piles has an important effect on the mobilized penetration resistance, where blunt or flat tips are typically associated with greater penetration resistances. High penetration resistances can lead to refusal at shallower depths than required or to structural damage during installation of piles. As described by Tovar-Valencia et al. (2021), the design of piles with flat bases often uses the results of Cone Penetration Test (CPT) soundings equipped with conical tips with an apex angle of 60°, without direct consideration of the effects of differences in pile geometry (Clausen et al. 2005; Lehane et al. 2005; Jardine et al. 2005; Salgado et al. 2011). This results in added uncertainty, especially considering that the tip shape effect may have a dependency on soil type and properties like density, tip surface roughness, overburden stress, and depth.

Durgunoglu and Mitchell (1973) presented analytical limit equilibrium solutions which indicated that penetration resistance increases with increases in tip apex angle, penetrometer surface roughness, soil friction angle, and depth in cohesionless soils. A number of subsequent numerical and experimental studies have also reported an increase in penetration resistance with increasing cone apex angle in sandy soils (e.g., Lobo-Guerrero and Vallejo 2007; Lin and Wu 2013; Wu and Yamamoto 2014; Tovar-Valencia et al. 2021). The fall cone test is also routinely employed to estimate the shear strength of clayey soils. In this method, the effect of the cone apex angle can be considered by means of analytical solutions (Hansbo 1957; Houlsby 1982). Wood (1985), Kuomoto and Houlsby (2001), and Dastider et al. (2021) performed fall cone experiments and simulations and reported an increase in penetration depth, corresponding to a decrease in penetration resistance, for sharper tips.

Research on tip shape effects can also be found in the field of bio-inspired geotechnics, which consists of the adaptation of biological strategies towards geotechnics applications and has received recent and growing interest (Martinez et al. 2021). Researchers from the biological sciences have addressed the tip shape effects from an evolutionary perspective. For example, Mishra et al. (2018) performed experiments and simulations on penetrometers with different shapes, including flat and conical tips and tips with morphology inspired by plant roots. The authors reported that the plant-inspired penetrometer and those with conical tips generated the smallest penetration resistances. Berhmann and Berry (2021) performed experiments on penetrometers of varying apex angles to shed light on the burrowing adaptations of sand-diving lizards. The authors also reported a decrease in penetration resistance as apex angle decreased. The tip of the stingers and egg-laying organs of honeybees, mosquitoes, and wasps have been shown to have a small apex angle. It has been hypothesized that these "streamlined" shapes helps reduce the penetration resistance in solid substrates (Kong and Wu 2009; Ling et al. 2016; Cerkvenik et al.2017).

Despite the evidenced importance of the tip shape on the mobilized penetration resistances and induced failure mechanisms, a relationship based on experimental or numerical results between the apex angle of conical tips and their penetration resistance is still to be developed. Additionally, little attention has been devoted to the effects in both shallow and deep penetration conditions. This paper combines the results of two investigations on the effect of the apex angle on the penetration resistance to provide additional data and characterize the failure mechanisms during both shallow and deep penetration conditions. The first investigation consists of Discrete Element Modeling (DEM) simulations which explicitly model and track each particle in a granular assembly and enable a meso-scale analyses of the failure mechanisms in terms of particle displacements and stress changes. The second investigation consists of penetration tests in a geotechnical centrifuge which achieve overburden stress levels representative of field conditions.

2. Materials and methods

This section provides a brief description of the DEM simulations and centrifuge tests performed; the complete methods used in both numerical and physical models are detailed in Chen et al. (2021) and O'Hara and Martinez (2022a). Penetration conditions are considered shallow when the soil exhibits a failure mechanism that propagates to the soil free surface (i.e., heaving) and the increase in penetration resistance with depth is parabolic or quasi-linear. Penetration conditions are considered deep when the failure mechanism is localized around the penetrometer's tip. Fig. 1 shows schematics of the penetration conditions, where the transition from a shallow to deep penetration mechanism takes place at the critical depth (Z_{crit}).

2.1. DEM simulations

The numerical simulations were performed using the PFC3D 5.0 software (Itasca Inc.). DEM was used in this investigation because it has the ability to model large deformation processes without numerical stability issues, it provides a rich dataset from each simulation at particle, meso, and macro spatial scales, and it does not assume that coarse-grained soils are continuum materials. The simulations employ spherical particles whose interactions follow the linear contact model with rolling resistance, which has been shown to successfully simulate the response of sub-rounded to sub-angular soil (Ai et al. 2011; Wensrich and Katterfeld 2012; McDowell et al. 2012). During the simulations, the particle displacements and contact forces are computed at each calculation step (Cundall and Strack, 1979). Fig. 2(a) shows the grain size distribution of the simulated granular assembly, which is upscaled from the "Mix B" soil in Kuei et al. (2020). The mean particle size (D_{50}) is 0.0144 m, the coefficient of uniformity (C_U) is 1.2, and the coefficient of curvature (C_C) is 0.96. The larger particle size with respect to natural soils enables reducing the computational cost of the simulations, as previously employed in numerous investigations (e.g., O'Sullivan 2011; Roessler and Katterfeld 2018; Coetzee 2019). Table 1 presents the model parameters, which include a normal stiffness (k_n) of 1.65E+06 N/m, shear stiffness (k_s) of 1.10E+06 N/m, particle friction coefficient (μ) of 0.4, rolling friction coefficient (μ_{rr}) of 0.4, probe–particle friction coefficient of 0.3, and ball–chamber friction coefficient (μ') of 0.1. The modeling parameters were calibrated to produce a behaviors typical of a sub-rounded to sub-angular poorly-graded sand during triaxial compression and cone penetration testing simulations. Further information regarding the determination of the modeling parameters can be found in Kuei et al. (2020) and Chen et al. (2021), who previously used the same simulation parameters in triaxial and penetration simulations.

Drained triaxial compression simulations were performed on cubic specimens with side length of 0.412 m to explore the element-level behavior of the simulated particles. In these simulations, the rigid lateral walls maintained a constant-stress boundary using a servo-control algorithm while the vertical walls compressed the specimen. The specimens had an initial void ratio (e_0) of 0.61 and were subjected to confining stresses (σ'_3) of 5, 25, 100, and 400 kPa. Fig. 2(b) shows the greater deviatoric stresses (q) mobilized by the specimens subjected to greater confining stresses. In terms of the ratio of deviatoric to mean effective stresses (q/p'), the specimens confined at smaller stresses mobilize greater peak values (Fig. 2(c)). However, all specimens converge to the same value at large strains (i.e., critical state value). The specimens confined at smaller stresses exhibit greater dilative volumetric strains (Fig. 2(d)). Finally, the test results indicate a failure envelope with a critical state friction angle, φ_{cs}, of 36° (Fig. 2(e)). These trends show that the simulation parameters are able to reproduce the expected behaviors of coarse-grained soils, including stress-dependency and stress-dilatancy. Additionally, Chen et al. (2021) presented results from CPT simulations at overburden stresses ranging from 5 to 400 kPa, indicating that the DEM model produces behaviors characteristic of medium-dense sands.

The penetration simulations were performed on virtual calibration chambers (VCCs) with a diameter ($D_{chamber}$) of 0.70 m and a height ($H_{chamber}$) of 0.65 m. The VCCs contained specimens with about 120,000 particles, and the assemblies had an e_0 of 0.61. Simulations were performed on unconfined and confined assemblies to model shallow and deep penetration conditions, respectively. The unconfined assembly was contained within a rigid VCC; however, the surface of the assembly was not constrained in order to allow for the development of a shallow failure mechanism (Fig. 3(a)). The simulations employ a gravitational constant of -9.81 m/s^2. The confined assemblies were contained within a VCC whose top and radial walls were stress-controlled, and these simulations did not consider gravitational effects. The top wall was servo-controlled to apply a constant stress of 100 kPa which prevented the upward flow of soil particles. The radial stress was controlled by a series of eight ring walls. Each ring wall was independently servo-controlled to maintain a radial stress of 50 kPa (Fig. 3(b)). As discussed in Chen et al. (2021), using ring walls rather than a single cylindrical wall allows a uniform radial stress to be maintained along the chamber height. The applied stresses to the confined sample result in an earth pressure coefficient (K) of 0.5, which is slightly greater than the expected K at rest conditions for the friction angle of the simulated particles. A total of 354 measurement spheres (MS) with a diameter of 0.033 m were placed along a vertical plane within each specimen to monitor the soil stresses, which remain stationary throughout the simulations. The ratio of the MS volume to particle volume is about 12. Fig. 3(c) shows the MS arrangement.

An important consideration in DEM penetration simulations is the relative size of the VCC to the probe, and of the probe to the particles. The probe used in all the simulations had a diameter (D_{probe}) of 0.044 m (cross sectional area of 15 cm^2), leading to a chamber diameter to probe diameter ratio ($D_{chamber}/D_{probe}$) of 15.9 and a probe diameter to mean particle size ratio (D_{probe}/D_{50}) of 3.1. A $D_{chamber}/D_{probe}$ of 15.9 has previously been shown by Khosravi et al. (2020) to reduce potential boundary effects, and this value is consistent with previous penetration simulations in 3D DEM (e.g., Arroyo et al. 2011; Butlanska et al. 2014; Zeng and Chen 2016; Ciantia et al. 2016 and 2019, with typical values between 6 and 16.9). While the D_{probe}/D_{50} value of 3.1 employed in DEM simulations is smaller than for typical field and experimental calibration chamber tests in sands, this is consistent with previous DEM simulations (e.g., Arroyo et al. 2011; Butlanska et al. 2014; Zeng and Chen 2016; Ciantia et al. 2016 and 2019, with typical values between 2.7 and 5.0). In addition, Khosravi et al. (2020) showed that while small D_{probe}/D_{50} values led to greater variations in measurements of penetration resistance (q_c), the value did not have a significant effect on the mean measured q_c value.

The penetration resistance was defined as the total vertical force acting on the probe tip divided by the tip's cross-sectional area, which is calculated as follows:

$$q_c = \frac{4\sum_{i=1}^{N_p} Q_{z,tip,i}}{\pi D_{probe}^2} \quad (1)$$

where $Q_{z,tip,i}$ is the vertical component of the contact normal or shear force i acting on the probe tip and N_p is the total number of tip–particle contacts.

Fig. 4(a) shows the geometry of the probe tips with varying apex angles used in the DEM simulations. The reported depth for the unconfined penetration simulations is measured relative to the center of the tip surface area to avoid biasing the results. Figure 4b shows probes with apex angles of 180° and 15° at the same position based on their center of surface area. This correction leads to a negligible effect on the results of the confined simulations due to the uniform stress conditions with depth. The probes were pushed into the specimens contained within the VCCs at a rate of 0.2 m/s. According to recommendations from O'Sullivan (2011) and Janda and Ooi (2016), the inertial number should remain at values smaller than $1\text{x}10^{-2}$ to ensure quasi-static conditions. Throughout both unconfined and confined simulations, the inertial numbers were smaller than $8.8\text{x}10^{-3}$. The overlaps between the particles was also tracked throughout the simulations, indicating that its magnitude remained smaller than 1% of the particles' radius.

2.2. Centrifuge testing

The centrifuge tests were performed at the Center for Geotechnical Modeling (CGM) at the University of California Davis on the 9-m radius centrifuge. Centrifuge tests can eliminate some of the limitations inherent to DEM simulations, such as the smaller $D_{chamber}/D_{probe}$ and D_{probe}/D_{50} ratios. The tests were performed at an acceleration of 30 times Earth's gravity (i.e., $N = g_{model}/g_{prototype} = 30$). The penetration tests were performed with probes equipped with 30°, 60°, 90°, 120°, and 180° tips (Fig. 4(c)). The probes had a model diameter (D_{probe}) of 19.05 mm and were instrumented with internal strain gages and a strain gage located behind the tip shoulder was used to measure q_c. The probes were inserted into the sand model using a hydraulic actuator at a rate of 2 mm/s.

The penetration tests were performed in a flexible-shear beam centrifuge container with dimensions of 1.651 m by 0.787 m. The sand model was prepared by air pluviation to a target relative density (D_R) of 65%. As discussed in more detail in O'Hara and Martinez (2022a), the resulting D_R was estimated between 61 and 64%. The model was constructed using Ottawa F65 sand, which is a poorly-graded subrounded silica sand that has been previously used by numerous researchers at the CGM. The grain size distribution of the Ottawa F65 sand is shown in Fig. 5(a). The sand has a D_{50} of 0.20 mm, C_U of 1.71, C_C of 1.00, maximum and minimum void ratios (e_{max} and e_{min}) of 0.78 and 0.51, respectively, and a critical state friction angle of 29.6° (Martinez et al. 2019). The ratio of probe diameter to mean particle size (D_{probe}/D_{50}) was 95, which falls within typical recommendations to avoid grain size effects (Fioravante 2002; Garnier & König 1998; Bolton et al. 1999).

Six penetration tests were performed to target depths of 0.318 m (prototype scale depth, Z, of 9 m, Z/D_{probe} of 16.7) at the locations shown in Fig. 5(b). The distance between any two tests was greater than or equal to 10 times D_{probe}. Three Cone Penetration Test (CPT) soundings with a probe diameter (D_{CPT}) of 10 mm were also performed in the model to assess possible spatial variability. Fig. 5(c) shows the depth profiles, which have similar q_c with depth particularly at depths smaller than 8 m. Fig. 5(d) shows a depth profile of the average tip resistance ($q_{c,average}$) along with profiles of $q_{c,average}$ ± one standard deviation (σ), showing the near negligible variability in q_c at depths smaller than 8 m.

This paper reports centrifuge results in prototype scale. Based on the scaling laws, the prototype length and depth scale with N ($L_{protoype} = L_{model}\ x\ N$, $Z_{protoype} = Z_{model}\ x\ N$), prototype stress is independent of N ($\sigma_{prototype} = \sigma_{model}$), and prototype force is scaled with N^2 ($F_{prototype} = F_{model}\ x\ N^2$) (Taylor 1995; Garnier et al. 2007).

3. Effect of cone apex angle on penetration resistance magnitude

Penetration profiles from DEM simulations performed in the unconfined and confined assemblies, which respectively model shallow and deep penetration conditions, are presented first. Second, results from the centrifuge tests are provided. Finally, the numerical and experimental results, along with results reported in the literature, are synthesized to quantify the relationship between tip apex angle and penetration resistance at different penetration depths.

3.1. Penetration profiles from unconfined and confined DEM simulations

The penetration simulations performed on the unconfined assemblies exhibited a quasi-linear increase in q_c with depth for all probe apex angles, as shown in Fig. 6, where the secondary axis of the plots indicates the corresponding Z/D_{probe} values. The depth is reported with respect to the center of the tip surface area, as described in Fig. 4(b). This increase of q_c with depth is due to the gravity-induced stress gradient and is typical of a shallow failure mechanism (i.e., Kim et al. 2016). All the profiles show a steady increase in q_c up to magnitudes between 1 and 2 MPa. The depth profiles are accompanied with local magnitude variations, which are an artifact of the upscaled particle sizes employed in these simulations, as previously described. However, they do not have a significant influence on the average q_c value, as indicated by Khosravi et al. (2020). In general, the q_c magnitude at any given depth increases as the cone apex angle is increased. These trends are described in more detail in the last part of this section.

The simulations performed in the confined assembly exhibit a relatively constant q_c value at depths greater than about 0.05 m, as shown in Fig. 7. The constant q_c values are due to the uniform stresses applied by the chamber top and radial walls and the absence of gravity in these simulations. However, the increase in q_c between depths of 0 and 0.05 m is due to the presence of the top chamber wall which applies a constant-stress boundary conditions. The q_c magnitudes are between 4 and 8 MPa, with the lower values corresponding to the probes with apex angles of 15° and 30° and the greater values corresponding to probes with apex angles of 150° and 180°. The 15° apex angle probe generally mobilizes greater q_c values than the 30° apex angle probe. This is attributed to the greater surface area of the sharper tip, which is 98% greater than that of the 30° apex angle probe. This observation was also reported by Lin and Wu (2012). The simulation with an apex angle of 60° yielded an average q_c of 4.6 MPa (obtained from the shaded region in Fig. 7). The associated normalized tip resistance (defined as $Q = (q_c - \sigma_{v0}) / \sigma'_{v0}$) is 45.0, which falls in the typical range for clean sands according to the soil behavior type chart from Robertson (2016).

3.2. Penetration profiles from centrifuge tests

The centrifuge penetration tests were performed to a prototype depth of 10.0 m, equivalent to a Z/D_{probe} of 16.7. The q_c profiles are reported as a function of depth with respect to the tips' center of surface area and the secondary y-axis indicates the corresponding Z/D_{probe} values. Fig. 8(a) presents the q_c profiles at shallower depths while Fig. 8(b) presents the entire profiles. All the tests show an increase in q_c with depth. At shallower depths, the q_c magnitudes at any given depth increase as the tip apex angle is increased (Fig. 8(a)). At greater depths, the effect of the tip apex angle appears to diminish (Fig. 8(b)) such that for Z/D_{probe} values greater than about 8 the depth profiles are indistinguishable from each other. The method described by Gui et al. (1998) and Kim et al. (2016) was used to estimate Z_{crit} values. In this method, Z_{crit} is defined as the depth where the term $q_c/(\sigma'_v P_a)^{0.5}$, where P_a is the atmospheric pressure, becomes constant. The Z_{crit} values determined from the depth profiles are between 6.5 and 7.0 m, corresponding to Z_{crit}/D_{probe} values between 11.4 and 12.2, as shown by the shaded region in Fig. 8(b). Kim et al. (2016) showed that the Z_{crit}/D_{probe} value depends on sand D_R. The authors performed CPT soundings in a silica sand with a D_R of 65% and reported a Z_{crit}/D_{CPT} value of about 12, which is in agreement with the results reported in this paper.

3.3. Relationship between penetration resistance magnitude and cone apex angle

The penetration resistances from the DEM and centrifuge investigations indicate a general increase in penetration resistance with increases in the tip apex angle. The results of the DEM simulations are summarized in Figs. 9(a–c). The q_c values are reported for Z/D_{probe} values of 2 and 5 for the unconfined simulations (the reported q_c values are averages obtained from a depth range equal to 1 D_{probe}; for example, for a Z/D_{probe} of 2, the average q_c is obtained from depths of 1.5 to 2.5 D_{probe}), and for the confined simulations the average q_c is obtained for the shaded depths in Fig. 7 which correspond to the last 0.044 m of penetration (i.e. equal to 1 D_{probe}) to avoid the effects of the top constant-stress chamber boundary. Fig. S1 presents a comparison of the bearing capacity factors ($N_q = q_c/\sigma_v'$) calculated from the q_c from the confined DEM simulations with various analytical and semi-analytical solutions, showing that the values are within the range for the Janbu (1976) solution.

The relationships between q_c and cone apex angle for the centrifuge tests are presented in Figs. 10(a–c). Results are provided for Z/D_{probe} of 2, 5, and 15, which respectively correspond to shallow, intermediate, and deep penetration conditions. The reported values are averages obtained from a depth interval of 1 D_{probe}, as previously described for the DEM simulations. The q_c increases with increasing apex angle at Z/D_{probe} of 2 and 5. At Z/D_{probe} of 15, however, the q_c values are independent of the apex angle. Fig. S1 presents the N_q values calculated from the q_c from the centrifuge tests at Z/D_{probe} of 15 and centrifuge CPT tests at Z/D_{CPT} of 15. The figure shows that the centrifuge N_q values are between the predictions from the Durgunoglu and Mitchell (1973) and Vesic (1977) solutions.

The data from the DEM simulations and centrifuge tests is presented in terms of the q_c at any given apex angle ($q_{c,i}$) normalized by the q_c of the probe with a 60° tip ($q_{c,60°}$) in Figs. 9(d–f) and 10(d–f). For the simulations, the value of $q_{c,i}/q_{c,60°}$ increases by a greater amount for the shallower depths, with values as high as 1.9 for a Z/D_{probe} of 2, followed by values as high as 1.4 for a Z/D_{probe} of 5, and 1.2 for the confined simulations. The centrifuge results also show a greater increase with apex angle for the shallowest depth of Z/D_{probe} of 2, with values as high as 1.4. The $q_{c,i}/q_{c,60°}$ reaches values as high as 1.1 at a Z/D_{probe} of 5, whereas $q_{c,i}/q_{c,60°}$ does not change significantly with apex angle at a Z/D_{probe} of 15. In general, the $q_{c,i}/q_{c,60°}$ values from the simulations and experiments appear to be relatively constant at apex angles between 30° and 60°, increase more sharply at apex angles between 60° and 120°, and reach relatively stable values at angles between 120° and 180.

Values reported in the literature also show an increase in q_c with increasing apex angle. In order to compare the results from different studies, $q_{c,i}/q_{c,60°}$ are reported in Fig. 11(a–c), where $q_{c,60°}$ from each study is used in the normalization. Lobo Guerrero and Vallejo (2007) and Lin and Wu (2012) performed DEM simulations on unconfined assemblies, whereas Wu and Yamaoto (2014) performed Finite Element Modeling (FEM) simulations in a confined specimen. While none of these studies investigated a wide range of apex angles, the three datasets show an increase in $q_{c,i}/q_{c,60°}$ with increasing apex angle (Fig. 11(a)). The data generally shows small changes at apex angles between 30° and 40° and greater changes at angles between 60° and 120°. Tovar-Valencia et al. (2021) performed penetration experiments in a calibration chamber on medium dense and dense silica sand using probes with apex angles of 60° and 180°. The results indicate an increase in $q_{c,i}/q_{c,60°}$ with apex angle in both medium dense and dense sand (Figs. 11(b and c)). The results show greater increases in $q_{c,i}/q_{c,60°}$ at shallower depths, with values as high as 2.0 for a Z/D_{probe} of 2 and as high as 1.4 for a Z/D_{probe} of 10.

As previously described, Durgunoglu and Mitchell (1973) presented limit equilibrium solutions of penetration resistance in shallow conditions. The solutions for cohesionless soils are in terms of the bearing factor $N_{\gamma q}$ ($q_c = \gamma_s D_{probe} N_{\gamma q} \xi_{\gamma q}$, where γ_s is the soil buoyant unit weight and $\xi_{\gamma q}$ is a shape factor). Fig. 11(d) presents bearing factors for a semi-rough penetrometer (ratio of interface to soil friction angles (δ/φ) of 0.5) at Z/D of 2 and 5. The values are presented in normalized form as the ratio of the bearing factor for any given apex angle ($N_{\gamma q,i}$) to the bearing factor for an apex angle of 60° ($\mathrm{N}_{\gamma q,60°}$). While the $N_{\gamma q,i}/N_{\gamma q,60°}$ parameter is equal to the $q_{c,i}/q_{c,60°}$ for a given soil and penetrometer, the values are presented in terms of $N_{\gamma q,i}/N_{\gamma q,60°}$ for consistency with the original solutions. The $N_{\gamma q,i}/N_{\gamma q,60°}$ values show similar trends as those previously described, with values that increase with cone apex angle. Additionally, the increases observed at small angles (i.e., 30° to 60°) are smaller than those at greater angles (i.e., 90° to 150°).

The results from the DEM simulations and centrifuge penetration tests (Figs. 9 and 10), along with those presented in the literature (Fig. 11), exhibit the following trends: (i) increase in q_c with increasing apex angle, (ii) greater rates of q_c increase at apex angles between 60° and 120°, and (iii) a smaller increase in q_c with apex angle as the depth is increased. A logistic equation in terms of $q_{c,i}/q_{c,60°}$ is proposed to capture the functional form of the relationship between apex angle and q_c, as follows:

$$\frac{q_{c,i}}{q_{c,60°}} = A + \frac{\left(\frac{q_{c,max}}{q_{c,60°}} - \frac{q_{c,min}}{q_{c,60°}}\right)}{1+\left(\frac{\alpha}{I}\right)^{-k}} \quad (2)$$

where $q_{c,min}$ and $q_{c,max}$ are the respective minimum and maximum values of the relationship between q_c and cone apex angle, α is any given apex angle, A is taken equal to the minimum $q_{c,i}/q_{c,60°}$ value, k is a fitting parameter controlling the rate of increase, and I is a fitted parameter controlling the inflection point of the function. In this equation, $q_{c,min}/q_{c,60°}$, $q_{c,max}/q_{c,60°}$, and A control the range of $q_{c,i}/q_{c,60°}$ values, and I and k control the shape of the curve.

Figs. 9(d–f) and 10(d–f) show Eq. (2) fitted to the DEM and centrifuge data, where the $q_{c,min}$ and $q_{c,max}$ values correspond to the minimum and maximum q_c values in each dataset. As shown, Eq. (2) provides a satisfactory fit to the data, with normalized root mean square values falling below 0.2 except for the centrifuge results at Z/D_{probe} = 15, with a value of 0.47. Table 2 provides a summary of the parameters used in the logistic fits. The k and I parameters decrease as the Z/D_{probe} is increased for both DEM and centrifuge results due to the smaller increase in q_c with apex angle and the change in inflection point to smaller apex angles with increasing depth. Eq. (2) is fitted to the normalized bearing factors from Durgunoglu and Mitchell (1973), which also show a high-quality fit to the analytical results. Fitted equations are not included in Figs. 11(a–c) because the results reported in any one study do not cover the entire range of apex angles.

4. Meso-scale analysis of apex angle effects from DEM simulations

The mobilized penetration resistance depends on the induced soil deformations and state of effective stresses around the penetrometer. Since the cone apex angle was shown to influence the mobilized q_c, it follows that it must also induce different deformations or stress changes within the particles in the vicinity of the tip. This is investigated using the DEM simulation results by means of particle displacement and soil stress measurements. Analysis is performed in both unconfined and confined simulations on probes with apex angles of 30°, 60°, 120°, and 180°.

4.1. Unconfined shallow penetration

As the tip apex angle was increased, greater particle displacements were induced during penetration. Fig. 12(a) shows this in terms of absolute particle displacements, where the particle color represents the displacement magnitude. These results show greater displacements around the tips with angles of 120° and 180°. Additionally, the figures show heaving of the assembly free surface, as expected for a shallow penetration process. Fig. 12(b) presents vectors of incremental particle displacement, whose color and size are proportional to the particle displacement magnitude, obtained from penetration depths corresponding to Z/D_{probe} of 0 to 2. These results also show the increase in particle displacements as the apex angle is increased as well as the lateral particle displacements associated with a shallow failure. The particles contacting the probe tips have displacement vectors with directions that are close to normal to the tip surface. This results in particle trajectories that are close to vertical for the 120° and 180° tips, likely because particles become trapped below the probe tips.

The magnitude and spatial distributions of soil stresses around the probes are also influenced by the tip apex angle. Figs. 13(a and d) show spatial maps of radial (σ'_r) and vertical effective stresses (σ'_z), respectively, obtained from the measurement spheres shown in Fig. 3(c). The results indicate that the magnitude of both σ'_r and σ'_z below the probe tips increases as the apex angle is increased. Additionally, the size of the zone with larger effective stresses also increases with apex angle. The mean effective stresses (p') and circumferential effective stresses (σ'_ϑ) showed similar trends as described for σ'_r and σ'_z; however, these are not included here for brevity.

The relative difference between the major (σ'_1) and minor (σ'_3) principal effective stresses as well as their orientation is visualized in the spatial cross diagram presented in Fig. 14(a). In these diagrams, the longer line represents the relative magnitude and orientation of σ'_1 and the shorter line represents the relative magnitude and orientation of σ'_3, and each diagram is normalized by the largest σ'_1 value in the simulation with an apex angle of 180°. As shown, the length of the crosses close to the probe tips increases as the apex angle is increased, indicating an increase in σ'_1 and σ'_3, in agreement with the spatial σ'_r and σ'_z maps. Figs. 14(b and c) show σ'_r and σ'_z measurements obtained from locations below and around the tip, as indicated in Fig. 3(c), for probes with apex angles between 15° and 180°. The results show the differences in induced stress changes, with the stresses below the tip increasing as the apex angle is increased, and with σ'_z constantly being greater than σ'_r. In contrast, both σ'_r and σ'_z at locations around the tip decrease as the apex angle is increased, and σ'_r is greater σ'_z. These results suggest that the soil below the tips fails under axial compression, and this effect is more apparent for the blunt tips. On the other hand, the soil around the tips fails under lateral compression, which is more apparent for the sharp tips.

The results of this meso-scale analysis indicate that the shallow failure mechanism around the probe is influenced by the cone apex angle, where probes with more blunt tips induce greater particle displacements and effective stress changes. These trends can provide an explanation for the increase in q_c with apex angle in shallow conditions, as shown in Figs. 9(a), 10(a), and 11. Additionally, the meso-scale analysis indicates that the magnitudes and distributions of soil stresses, σ'_r, σ'_z, σ'_1, and σ'_3 are qualitatively similar for the probes with apex angles of 30° and 60° as well as for the probes with apex angles between 120° and 180°. In contrast, greater changes are observed between the probes with apex angles between 60° and 120°: (i) at an angle of 120° particles get trapped below the tip while at 60° the particles flow around the tip, (ii) the σ'_r and σ'_z magnitudes and distributions increase considerably between the 60° and 120° probes, and (iii) the relative magnitudes and orientations of the principal effective stresses also change significantly between the 60° and 120° probes.

4.2. Confined deep penetration

In the confined assembly, the probes with greater apex angles induced greater particle displacements, as shown in Figs. 15(a and b) in terms of absolute particle displacements and incremental particle displacement vectors, respectively. The latter presents displacements obtained from penetration depths corresponding to Z/D_{probe} of 8 to 10 within the confined assembly. Similar to the unconfined penetration simulations, the probes with apex angles of 120° and 180° induced significantly greater particle displacements with directions close to vertical, likely due to trapping of particles below the tip. In contrast, the displacements induced by probes with apex angles of 30° and 60° have greater horizontal components as compared to those induced by the probes with apex angles of 120° and 180°, as shown in the insets in Fig. 15(a–d).

The spatial maps of σ'_r and σ'_z presented in Figs. 16(a and b) show similar trends as previously described for the unconfined simulations, where the blunter tips induce greater increases of stresses in zones with greater sizes around the probe tips. The distributions of p' and σ'_ϑ show similar trends; however, they are not included here for brevity. The probes with sharp and blunt angles show different trends in the distributions of large σ'_r and σ'_z magnitudes. The sharper tips induce greater increases in σ'_r at locations around the tips (Fig. 16(a)) whereas the blunter tips induce greater increases in σ'_z at locations below the tips (Fig. 16(b)). These trends are in qualitative agreement with the particle displacement directions shown in Fig. 15(b). Fig. 17(a) shows spatial cross diagrams that indicate the relative magnitude and orientation of σ'_1 and σ'_3, where the length of the lines is normalized by the greatest σ'_1 value in the 180° simulation. The figures show that σ'_1 has orientations close to horizontal at locations laterally around the tips with apex angles of 30° and 60°, as shown in the insets in Fig. 17(a). For the probes with 120° and 180° tips, σ'_1 is more vertically-aligned at locations below the tips. Figs. 17 (b and c) show σ'_r and σ'_z at locations below and around the tip, respectively, as indicated in Fig. 3(c). The results show similar trends as those for the unconfined simulations, where both σ'_r and σ'_z increase as the apex angle is increased below the tip, while both stresses decrease with increasing apex angle. Below the tip, the σ'_z magnitudes are greater, indicating failure under axial compression. Around the tip, the σ'_r magnitudes are greater, indicating failure under axial compression.

The results of the meso-scale analysis are in agreement with the q_c measurements in confined conditions, where the q_c increased with apex angle (Figs. 9 (c and f)). This increase was smaller than that observed in the unconfined conditions (Figs. 9(a and d)). The particle displacements and changes in states of stress in Figs. 12 (a and b), Fig. 13, and Figs. 14 (a to c) indicate that in the confined assembly, the sharp tips act like a wedge, inducing a lateral compression failure of the soil around the tip. Similar to the results for the unconfined simulations, the induced particle displacements and stress changes change more dramatically between the probes with apex angles between 60° and 120°.

5. Conclusions

Numerical and experimental investigations were performed to address the effects of penetrometer tip apex angle on the mobilized penetration resistance, q_c. DEM penetration simulations were performed in unconfined and confined granular assemblies calibrated to reproduce the behavior of sub-rounded sands, and centrifuge penetration experiments were performed in a fine silica sand at an acceleration of 30 g. The effects of tip apex angle on q_c were evaluated in shallow penetration conditions at a depth to probe ratio, Z/D_{probe}, of 2, as well as in deep penetration conditions either in a confined assembly in DEM or at Z/D_{probe} greater than 12 in the centrifuge tests.

While the results of both DEM simulations and centrifuge tests indicate an increase in q_c as the tip apex angle is increased, greater increases in q_c with apex angle were observed in shallow penetration conditions than in deep conditions. The changes in q_c magnitude at apex angles between 30° and 60° and between 120° and 180° were modest, while greater changes in q_c were observed at apex angles between 60° and 120°. For shallow conditions, the ratio of q_c mobilized by the 180° tip to that mobilized by the 60° tip was between 1.9 and 1.4; for deep conditions, this ratio was between 1.2 and 1.0. A review of previously published experimental, numerical, and analytical results supports the trends obtained in this investigation between q_c and tip apex angle. Based on the DEM, centrifuge, and literature results, a logistic function is found to successfully capture the functional form of the relationship between q_c and tip apex angle in sands.

A meso-scale analysis of the particle displacement and effective stress changes induced during shallow and deep penetration was performed on the DEM results. This analysis indicates that penetration with blunter tips (i.e., those with greater apex angle) induces greater particle displacements, partly due to trapping of particles at locations below the tip, as compared to sharper tips (i.e., those with smaller apex angle). The blunter tips also induce greater increases in radial and vertical effective stresses, and the changes in effective stresses take place in zones of larger size below the blunter tips. Further analysis of the changes in state of stresses indicates a change in the failure mechanism of the soil in close proximity to the tips. For the blunt tips, the soil below the tip fails in axial compression, where the major principal effective stress, σ'_1, is oriented close to the vertical direction. For the sharp tips, the soil around the tip fails in lateral compression, where the orientation of σ'_1 is closer to the horizontal direction. This difference in failure mechanism is more strongly visible in deep penetration conditions where the failure does not propagate to the soil free surface.

While the DEM simulations and centrifuge experiments provided consistent trends, the results indicate some differences. One salient difference is the observed increase in q_c with apex angle in the confined DEM simulations (Fig. 9(c)) that contrasts with the largely independent q_c magnitudes observed in deep penetration conditions in the centrifuge tests (Fig. 10(c)). This could be due to the absence of particle crushing in the DEM simulations, while crushing was readily visible in the centrifuge tests, the greater probe-to-particle ratio in the centrifuge tests, and the difference in diameter between the probes in the DEM and centrifuge tests. Nevertheless, the agreement of the reported trends to those in the literature lead to confidence in the results. These investigations considered medium-dense to dense sub-rounded poorly-graded quartz sands, so future exploration should consider the effects of relative density and gradation on the reported trends. Additionally, the possible effect of the probe diameter should be evaluated in future studies, as previous studies have pointed out their importance (i.e. Bolton et al. 1999; Kim et al. 2016). The proposed relationship between tip resistance and apex angle (i.e., Eq. 2) was determined based on a fitting exercise. Further research should be performed to evaluate the physical meaning of the fitting parameters (i.e., k and I) as well as the possible effect of depth, relative density, friction angle, and mineralogy on these parameters.

Data Availability Statement

All data, models, or codes generated or used during the study are available from the corresponding author by request. All data shown in the figures and tables can be provided on request.

Acknowledgements

This material is based upon work supported by the National Science Foundation (NSF) under Award No. 1942369 and by the Engineering Research Center Program of the NSF under Cooperative Agreement No. EEC-1449501. The centrifuge tests were conducted at the UC Davis CGM, which is supported under grant No. CMMI-1520581. Any opinions, findings and conclusions expressed in this material are those of the author(s) and do not necessarily reflect those of the NSF.

References

Ai, J., J. F. Chen, J. M. Rotter, and J. Y. Ooi. 2011. "Assessment of rolling resistance models in discrete element simulations." *Powder Technology* 206 (3): 269–282. https://doi.org/10.1016/j.powtec.2010.09.030.

Arroyo, M., J. Butlanska, A. Gens, F. Calvetti, and M. Jamiolkowski. 2011. "Cone penetration tests in a virtual calibration chamber." *Géotechnique* 61 (6): 525–531. https://doi.org/10.1680/geot.9.P.067.

Bergmann, P.J., and D. S. Berry. 2021. "How head shape and substrate particle size affect fossorial locomotion in lizards." *J. Exp. Bio.* 224.

Bolton, M. D., M. W. Gui, J. Garnier, J. F. Corte, G. Bagge, J. Laue, and R. Renzi. 1999. "Centrifuge cone penetration tests in sand." *Géotechnique* 49 (4): 543–552.

Butlanska, J., M. Arroyo, A. Gens, and C. O'Sullivan. 2014. "Multi-scale analysis of cone penetration test (CPT) in a virtual calibration chamber." *Canadian Geotechnical Journal* 51 (1): 51–66. https://doi.org/10.1139/cgj-2012-0476.

Cerkvenik, U., van de Straat, B., Gussekloo, S.W.S. and van Leeuwen, J.L. 2017. "Mechanisms of Ovipositor Insertion and Steering of a Parasitic Wasp." *Proc. Natl. Acad. Sci.* 114 (37): E7822–31. https://doi.org/10.1073/pnas.1706162114.

Ciantia, M.O., M. Arroyo, J. Butlanska, and A. Gens. 2016. "DEM modelling of cone penetration tests in a double-porosity crushable granular material." *Computers and Geotechnics* 73: 109–127. https://doi.org/10.1016/j.compgeo.2015.12.001.

Ciantia, M., C. O'Sullivan, and R. J. Jardine. 2019, September. "Pile penetration in crushable soils: Insights from micromechanical modelling." In *17th European Conference on soil Mechanics and Geotechnical Engineering (ECSMGE 2019). International Society for Soil Mechanics and Geotechnical Engineering.* https://doi.org/10.32075/17ECSMGE-2019-1111.

Chen, Y., A. Khosravi, A. Martinez, and J. DeJong. 2021. "Modeling the Self-Penetration Process of a Bio-Inspired Probe in Granular Soils." *Bioinspiration and Biomimetics* 16 (4): 046012. https://doi.org/10.1088/1748-3190/abf46e.

Clausen, C. J. F., P. M. Aas, and K. Karlsrud. 2005. “Bearing capacity of driven piles in sand, the NGI approach.” In Proc., Int. Symp. on Frontiers in Offshore Geotechnics (ISFOG 2005), edited by M. Cassidy and S. Gourvenec, 677–681. London: Taylor & Francis

Coetzee, C. J. 2019. “Particle upscaling: Calibration and validation of the discrete element method.” *Powder Technology* 344: 487–503. https://doi.org/10.1016/j.powtec.2018.12.022.

Cundall, P.A., and Strack, O.D.L. 1979. “A discrete numerical model for granular assemblies.” *Géotechnique* 29(1): 47-65

Dastider, A.G., S. Chatterjee, and P. Basu. 2021. “Advancement in estimation of undrained shear strength through fall cone tests.” *J. Geotech. Geoenviron. Eng.* 147 (7).

Durgunoglu, H.T. and Mitchell, J.K. 1973. “Static penetration resistance of soils.” *NASA Report* 14, 24.

Fioravante, V. 2002. “On the shaft friction modelling of non-displacement piles in sand.” *Soils Found.* 42 (2): 23–33.

Garnier, J., and D. Konig. 1998. “Scale effects in piles and nail loading tests in sand.” *Proc. Int. Conf. Centrifuge* 98, Tokyo, Balkema, Rotterdam, 1: 205–210.

Garnier, J., C. Gaudin, S. M. Springman, P. J. Culligan, D. Goodings, D. Konig, B. Kutter, R. Phillips, M. F. Randolph, and L. Thorel. 2007. “Catalogue of scaling laws and similitude questions in geotechnical centrifuge modelling.” *Int. J. Phys. Model. Geotech.* 7 (3): 01–23.

Gui, M. W., Bolton, M.D., Garnier, J., Corte, J.F., Bagge, G., Laue, J., and Renzi, R. 1998. “Guidelines for cone penetration tests in sand.” Proc., Int. Conf. on Centrifuge Modelling (Centrifuge ‘98), Vol. 1, A.A. Balkema, Rotterdam, Netherlands, 155–160.

Hansbo, S. 1957. “New approach to the determination of the shear strength of clay by the fall-cone test.” In Vol. 14 of Proc., Royal Swedish Geotechnical Institute, 1–48. Stockholm, Sweden: Swedish Geotechnical Institute.

Houlsby, G. T. 1982. “Theoretical analysis of the fall cone test.” *Géotechnique* 32 (2): 111–118. https://doi.org/10.1680/geot.1982.32.2.111.

Jardine, R., F. Chow, R. Overy, and J. Standing. 2005. “ICP design method for driven piles in sands and clays.” London: Thomas Telford, ICE Publishing.

Janbu, N. 1976. Static bearing capacity of friction piles, Proc. 6th Eur. *Conf. Soil Mech. Found. Eng.*, Vol. 1.2, 479–488.

Khosravi, A., A. Martinez, and J. T. DeJong. 2020. "DEM simulations of CPT measurements and soil classification." *Can. Geotech. J.* 57 (9): 1369–1387. https://doi.org/10.1139/cgj-2019-0512.

Kim, J. H, Y. W. Choo, D. J. Kim, and D. G. Kim. 2016. "Miniature cone tip resistance on sand in a centrifuge." *J. Geotech. Geoenviron. Eng.* 142 (3).

Kong, X. Q., and C. W. Wu. 2009. "Measurement and Prediction of Insertion Force for the Mosquito Fascicle Penetrating into Human Skin." *J. Bionic Eng.* 6 (2): 143–52. https://doi.org/10.1016/S1672-6529(08)60111-0.

Koumoto, T., and G. T. Houlsby. 2001. "Theory and practice of the fall cone test." *Géotechnique* 51 (8): 701–712. https://doi.org/10.1680/geot.2001.51.8.701.

Kuei, K. C., J. T. DeJong, and A. Martinez. 2020, February. "Particle Size Effects on the Strength and Fabric of Granular Media." In *Geo-Congress 2020: Modeling, Geomaterials, and Site Characterization,* 349–358. Reston, VA: American Society of Civil Engineers.

Lehane, B. M., J. Schneider, and X. Xu. 2005. "The UWA-05 method for prediction of axial capacity of driven piles in sand." In *Proc., of the Int. Symp. on Frontiers in Offshore Geotechnics* (IS-FOG 2005), 683–689. London: Taylor & Francis

Lin, J., and Wei W. 2012. "Numerical Study of Miniature Penetrometer in Granular Material by Discrete Element Method." *Philosophical Magazine* 92 (28–30): 3474–82. https://doi.org/10.1080/14786435.2012.706373.

Ling, J., L. Jiang, K. Chen, C. Pan, Y. Li, W. Yuan, and L. Liang. 2016. "Insertion and Pull Behavior of Worker Honeybee Stinger." *J. Bionic Eng.* 13 (2): 303–11. https://doi.org/10.1016/S1672-6529(16)60303-7.

Lobo-Guerrero, S., and L. E. Vallejo. 2007. "Influence of Pile Shape and Pile Interaction on the Crushable Behavior of Granular Materials around Driven Piles: DEM Analyses." *Granular Matter* 9 (3–4): 241–50. https://doi.org/10.1007/s10035-007-0037-3.

Martinez, A., S. Palumbo, and B. D. Todd. 2019. "Bio-Inspiration for anisotropic load transfer at soil-structure interfaces." *J. Geotech. Geoenviron. Eng.* 145 (10). https://doi.org/10.1061/(ASCE)GT.1943-5606.0002138.

Martinez, A., J. DeJong, I. Akin, A. Aleali, C. Arson, J. Atkinson, P. Bandini, T. Baser, R. Borela, R. Boulanger, M. Burrall, Y. Chen, C. Collins, D. Cortes, S. Dai, T. DeJong, E. Del Dottore, K. Dorgan, R. Fragaszy, D. Frost, R. Full, M. Ghayoomi, D. Goldman, N. Gravish, I. L. Guzman, J. Hambleton, E. Hawkes, M. Helms, D. L. Hu, L. Huang, S. Huang, C. Hunt, D. Irschick, H. Lin, B. Lingwall, W. A. Marr, B. Mazzolai, B. McInroe, T. Murthy, K. O'Hara, M. Porter, S. Sadek, M. Sanchez, C. Santamarina, L. Shao, J. Sharp, H. Stuart, H. H. Stutz, A. P. Summers, J. Tao, M. Tolley, L. Treers, K. Turnbull, R. Valdes, L. van Paassen, G. Viggiani, D. Wilson, W. Wu, X. Yu, and J. Zheng. 2021. "Bio-inspired geotechnical engineering: principles, current work, opportunities and challenges." *Geotechnique* http://doi.org/10.1680/jgeot.20.P.170.

McDowell, G. R., O. Falagush, and H. S. Yu. 2012. "A particle refinement method for simulating DEM of cone penetration testing in granular materials." *Geotechnique Letters* 2 (3): 141–147. https://doi.org/10.1680/geolett.12.00036.

Meyerhof, G.G. 1976. Bearing capacity and settlement of pile foundations. *J. Geotech. Eng. Div.,* 102(GT3).

Mishra, A. K., F. Tramacere, R. Guarino, N. M. Pugno, and B. Mazzolai. 2018. "A Study on Plant Root Apex Morphology as a Model for Soft Robots Moving in Soil." Edited by Josh Bongard. PLOS ONE 13 (6): e0197411. https://doi.org/10.1371/journal.pone.0197411.

O'Hara, K. B., and A. Martinez. 2022a. "Shaft and base capacity of snakeskin-inspired piles from centrifuge pile load tests." Accepted for publication in *GeoCongress* 2022.

O'Hara, K. B., and A. Martinez. 2022b. "Load transfer directionality of snakeskin-inspired piles during installation and pullout in sands." Submitted for possible publication in *J. Geotech. Geoenviron. Eng.*

O'Sullivan, C. 2011. "Particulate discrete element modelling: a geomechanics perspective" [M]. CRC Press. https://doi.org/10.11475/sabo.67.5_77.

Puech, A., and P. Foray. 2002. "Refined model for interpreting shallow penetration CPTs in sands." *Proc., Offshore Technology Conf.*, Houston.

Robertson, P. K. 2016. "Cone penetration test (CPT)-based soil behaviour type (SBT) classification system—an update." *Can. Geotech. J.* 53 (12): 1910–1927. https://doi.org/10.1139/cgj-2016-0044.

Roessler, T., and A. Katterfeld. 2018. "Scaling of the angle of repose test and its influence on the calibration of DEM parameters using upscaled particles." *Powder Technology* 330: 58–66. https://doi.org/10.1016/j.powtec.2018.01.044.

Salgado, R., S. I. Woo, and D. Kim. 2011. "Development of load and resistance factor design for ultimate and serviceability limit states of transportation structure foundations." FHWA/IN/JTRP-2011/03, SPR-3108. Washington, DC: Federal Highway Administration.

Taylor, R. N. 1995. "Geotechnical Centrifuge Technology." Chapman and Hall, London, UK.

Tovar-Valencia, R. D., A. Galvis-Castro, R. Salgado, and M. Prezzi. 2021. "Effect of Base Geometry on the Resistance of Model Piles in Sand." *J. Geotech. Geoenviron. Eng.* 147 (3): 04020180. https://doi.org/10.1061/(ASCE)GT.1943-5606.0002472.

Vesic, AS. 1977. Design of pile foundations. *Synthesis of Highway Practice 42*, Res. Bd., Washington DC.

Wensrich, C. M., and A. Katterfeld. 2012. "Rolling friction as a technique for modelling particle shape in DEM." *Powder Technology* 217: 409–417. https://doi.org/10.1016/j.powtec.2011.10.057.

Wood, D. M. 1985. "Some fall-cone tests." *Géotechnique* 35 (1): 64–68. https://doi.org/10.1680/geot.1985.35.1.64.

Wu, Y., and H. Yamamoto. 2014. "Numerical Analysis of the Effect of Pile Tip Shape on Soil Behavior around Pile." *Geotech. Eng. J.* SEAGS & AGSSEA45: 13.

Zeng, Z., and Y. Chen. 2016. "Simulation of soil-micropenetrometer interaction using the discrete element method (DEM)." Transactions of the ASABE, 59 (5): 1157–1163. https://doi.org/10.13031/trans.59.11726.

Table 1: DEM model parameters.

Parameter	Symbol	Value
Normal Stiffness (N/m)	k_n	1.65E+06
Shear Stiffness (N/m)	k_s	1.10E+06
Normal to Shear Stiffness Ratio	k_n/k_s	1.50
Particle Friction Coefficient	μ	0.4
Rolling Friction Coefficient	μ_{rr}	0.4
Probe–Particle Friction Coefficient	μ_p	0.3
Ball–Wall Friction Coefficient	μ'	0.1
Particle Density (kg/m^3)	G_s	2650
Local Damping	β	0.1

Table 2: Parameters for logistic fits.

Investigation	Penetration conditions	$q_{c,min}$ (MPa)	$q_{c,max}$ (MPa)	k	I
DEM	Unconfined, $Z/D_{probe} = 2$	0.27	0.49	5.2	142.5
	Unconfined, $Z/D_{probe} = 5$	0.83	1.22	3.4	137.2
	Confined	3.82	5.53	2.6	82.5
Centrifuge	$Z/D_{probe} = 2$	1.22	1.92	3.7	120.4
	$Z/D_{probe} = 5$	4.67	5.50	2.1	68.0
	$Z/D_{probe} = 15$	19.06	18.91	0.0	43.0

List of Captions

Table 1: DEM model parameters.

Table 2: Parameters for logistic fits.

Figure 1: Schematic of shallow and deep penetration conditions (adapted from Puech and Foray 2002 and Kim et al. 2016). Note: the size of the failure mechanisms are not drawn to scale.

Figure 2: (a) Grain size distribution of particles simulated in DEM. Results of isotropically-consolidated triaxial compression simulations as a function of axial strain on specimens with e_0 of 0.61: (b) deviatoric stress, (c) stress ratio, and (d) volumetric strain. (e) Failure envelope and Mohr circles at critical from triaxial compression tests.

Figure 3: DEM virtual calibration chambers for (a) unconfined and (b) confined penetration tests. (c) Measurement spheres used to monitor state of stresses (note: red spheres used to monitor stresses below the tip and blue spheres used to monitor stresses around the tip).

Figure 4: (a) Tips of varying apex angle used in DEM simulations. (b) Schematic of probes with 180° and 15° apex angle tips with their center of cone surface area at the same elevation. (c) Tips of varying apex angle used in centrifuge testing.

Figure 5: (a) Grain size distribution of the Ottawa F65 sand, (b) schematic of sand deposit used for centrifuge penetration tests and (c) CPT soundings performed in the model, and (d) average q_c and q_c ± one standard deviation.

Figure 6: Depth profiles of penetration resistances measured during unconfined DEM simulations for tips with apex angles of 15°, 30°, 45°, 60°, 90°, 120°, 150°, and 180°.

Figure 7: Depth profiles of penetration resistances measured during confined DEM simulations for tips with apex angles of 15°, 30°, 45°, 60°, 90°, 120°, 150°, and 180° (values in the shaded region are used to calculate average q_c values reported in Figure 8c).

Figure 8: Depth profiles of penetration resistances measured during centrifuge penetration tests with tips of varying apex angle for (a) depth smaller than 4 m (Z/D_{probe} smaller than 7.2) and (b) entire profile.

Figure 9: Absolute and normalized tip resistances measured in DEM simulations: (a) and (d) unconfined simulations at $Z/D_{probe} = 2$, (b) and (e) unconfined simulations at $Z/D_{probe} = 5$, and (c) and (f) confined simulations.

Figure 10: Absolute and normalized tip resistances measured in centrifuge penetration tests: (a) and (d) $Z/D_{probe} = 2$, (b) and (e) $Z/D_{probe} = 5$, and (c) and (f) $Z/D_{probe} = 15$.

Figure 11: Normalized tip resistances from: (a) Lobo Guerrero and Vallejo (2007), Lin and Wu (2012), and Wu and Yamamoto (2014), (b) Tovar-Valencia et al. (2021) on dense sand, and (c) Tovar-Valencia et al. (2020) on medium dense sand. (d) Normalized bearing factors from Durgunoglu and Mitchell (1973) for sand with a friction angle of 36°.

Figure 12: Particle displacements from unconfined DEM simulations with tips of varying apex angle at $Z/D_{probe} = 2$: (a) absolute particle displacements and (b) incremental particle displacement vectors.

Figure 13: Effective stresses from unconfined DEM simulations with tips of varying apex angle at $Z/D_{probe} = 2$: (a) radial and (b) vertical stresses.

Figure 14: (a) Major and minor principal stresses from unconfined DEM simulations with tips of varying apex angle at $Z/D_{probe} = 2$. Vertical and radial stresses (b) below and (c) around the tip from unconfined DEM simulations at $Z/D_{probe} = 2$.

Figure 15: Particle displacements from confined DEM simulations with tips of varying apex angle: (a) absolute particle displacements and (b) incremental particle displacement vectors.

Figure 16: Effective stresses from confined DEM simulations with tips of varying apex angle: (a) radial and (b) vertical stresses.

Figure 17: (a) Major and minor principal stresses from confined DEM simulations with tips of varying apex angle. Vertical and radial stresses (b) below and (c) around the tip from confined DEM simulations.

Figure S1: Comparison of bearing capacity factors from the DEM confined simulations, centrifuge tests at Z/Dprobe of 15, and centrifuge CPT tests at Z/DCPT of 15 with various analytical and semi-analytical solutions. η is the angle defining the geometry failure mechanism, Irr is the soil's rigidity index, and δ/φ is the ratio of cone-soil friction angle to soil internal friction angle. The Durgunoglu and Mitchell (1973) solution corresponds to a cone apex angle of 60°.

Table 1: DEM model parameters.

Parameter	Symbol	Value
Normal Stiffness (N/m)	k_n	1.65E+06
Shear Stiffness (N/m)	k_s	1.10E+06
Normal to Shear Stiffness Ratio	k_n/k_s	1.50
Particle Friction Coefficient	μ	0.4
Rolling Friction Coefficient	μ_{rr}	0.4
Probe–Particle Friction Coefficient	μ_p	0.3
Ball–Wall Friction Coefficient	μ'	0.1
Particle Density (kg/m^3)	G_s	2650
Local Damping	β	0.1

Table 2: Parameters for logistic fits.

Investigation	Penetration conditions	$q_{c,min}$ (MPa)	$q_{c,max}$ (MPa)	k	I
DEM	Unconfined, $Z/D_{probe} = 2$	0.27	0.49	5.2	142.5
	Unconfined, $Z/D_{probe} = 5$	0.83	1.22	3.4	137.2
	Confined	3.82	5.53	2.6	82.5
Centrifuge	$Z/D_{probe} = 2$	1.22	1.92	3.7	120.4
	$Z/D_{probe} = 5$	4.67	5.50	2.1	68.0
	$Z/D_{probe} = 15$	19.06	18.91	0.0	43.0

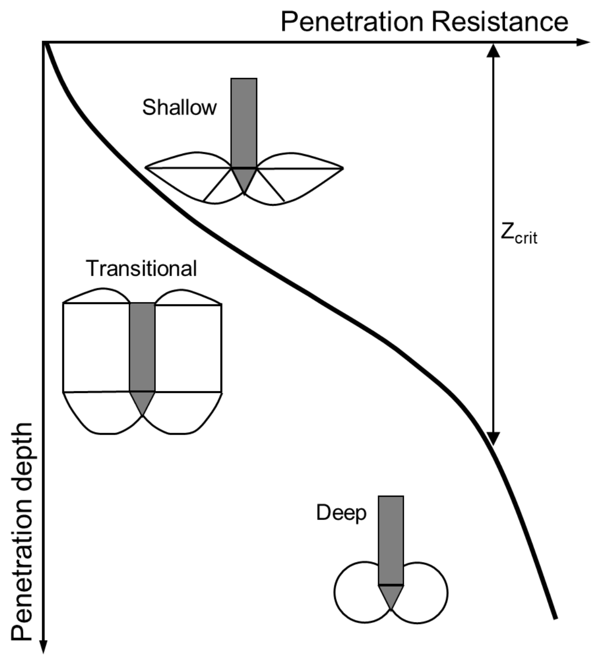

Figure 1: Schematic of shallow and deep penetration conditions (adapted from Puech and Foray 2002 and Kim et al. 2016). Note: the size of the failure mechanisms are not drawn to scale.

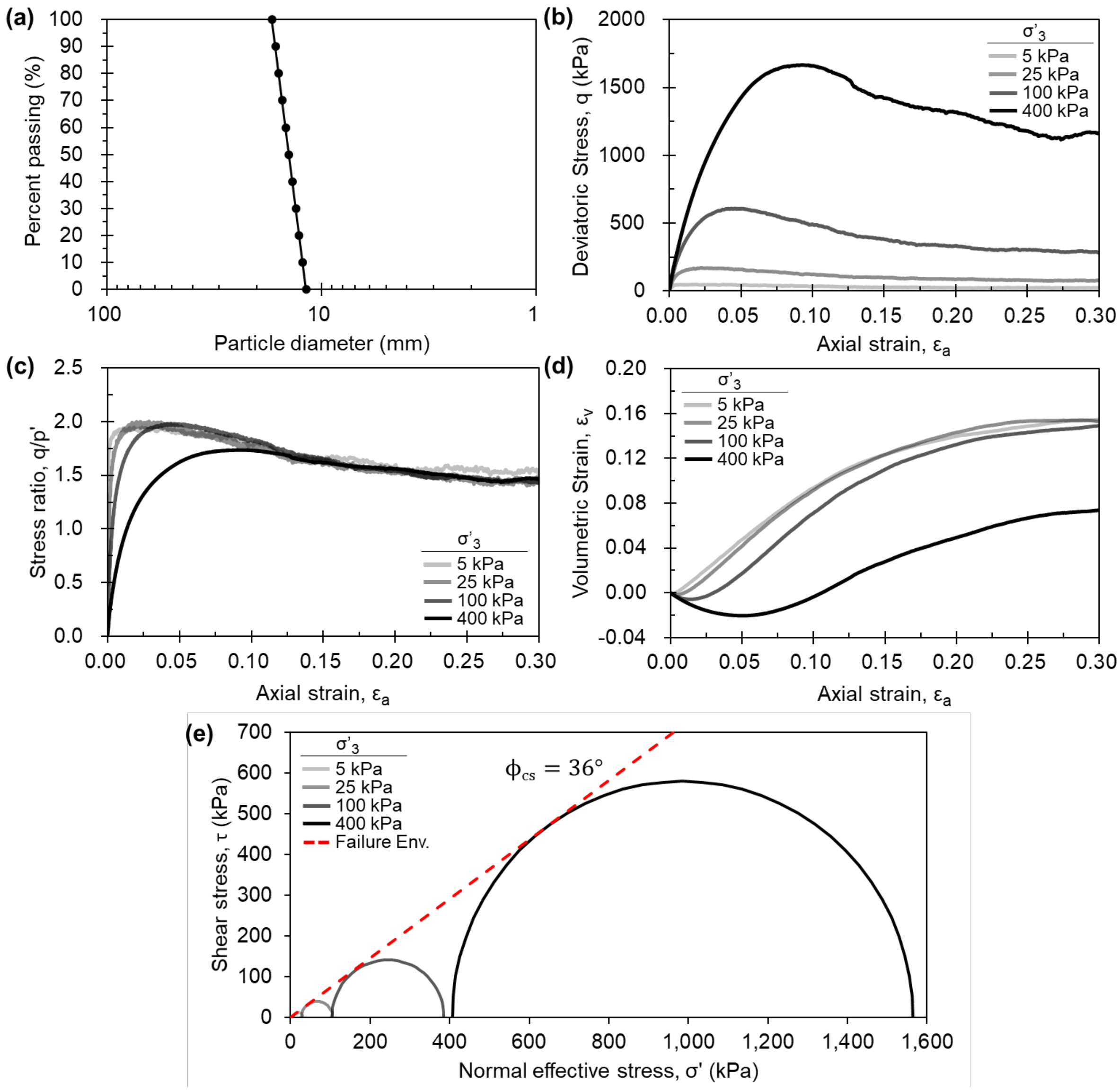

Figure 2: (a) Grain size distribution of particles simulated in DEM. Results of isotropically-consolidated triaxial compression simulations as a function of axial strain on specimens with e_0 of 0.61: (b) deviatoric stress, (c) stress ratio, and (d) volumetric strain. (e) Failure envelope and Mohr circles at critical from triaxial compression tests.

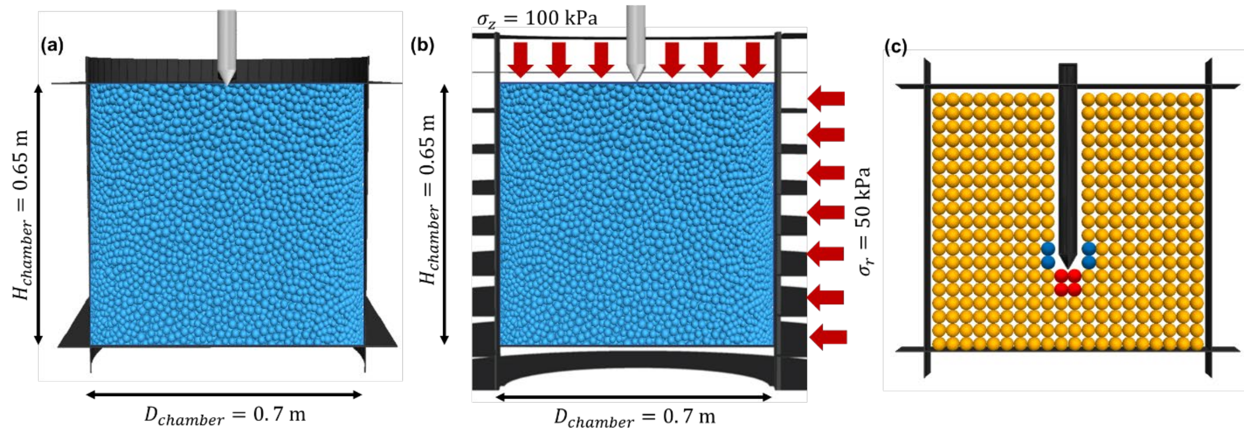

Figure 3: DEM virtual calibration chambers for (a) unconfined and (b) confined penetration tests. (c) Measurement spheres used to monitor state of stresses (note: red spheres used to monitor stresses below the tip and blue spheres used to monitor stresses around the tip).

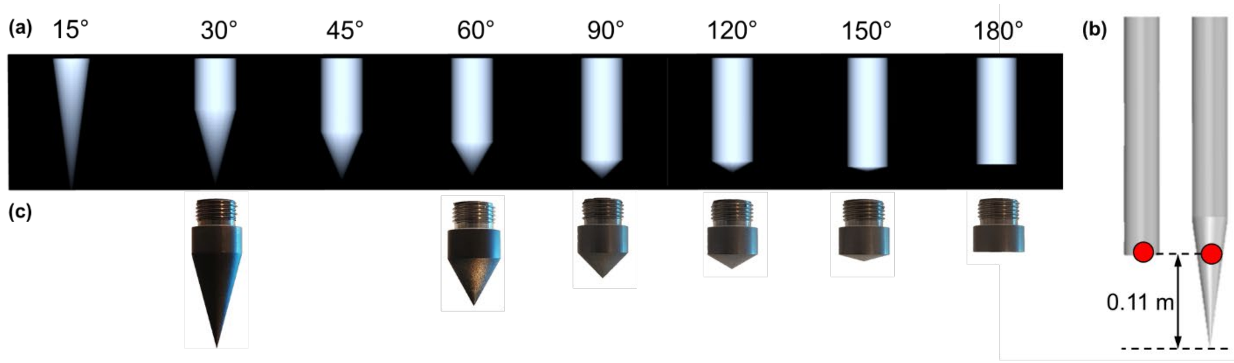

Figure 4: (a) Tips of varying apex angle used in DEM simulations. (b) Schematic of probes with 180° and 15° apex angle tips with their center of cone surface area at the same elevation. (c) Tips of varying apex angle used in centrifuge testing.

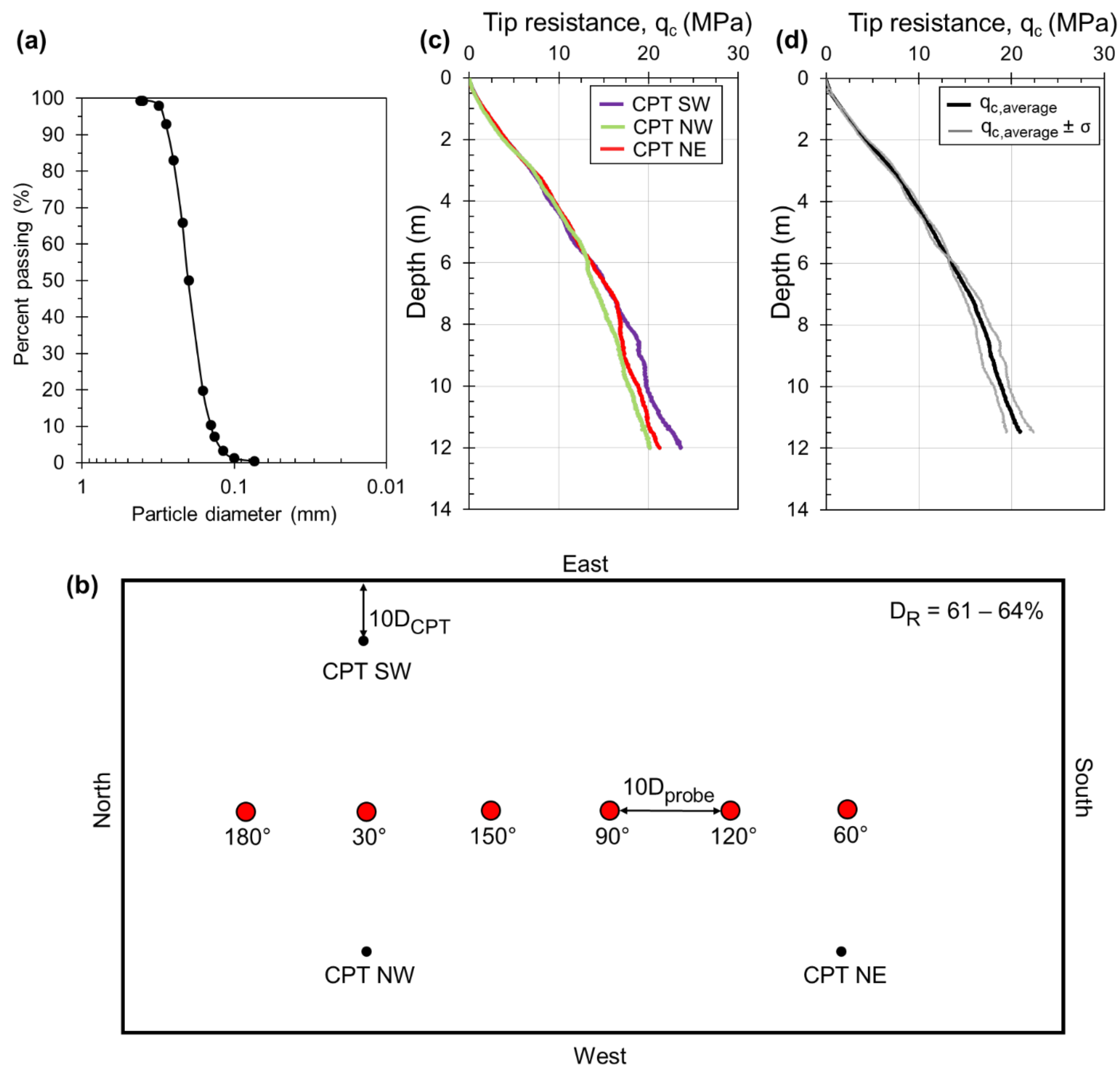

Figure 5: (a) Grain size distribution of the Ottawa F65 sand, (b) schematic of sand deposit used for centrifuge penetration tests and (c) CPT soundings performed in the model, and (d) average q_c and q_c ± one standard deviation.

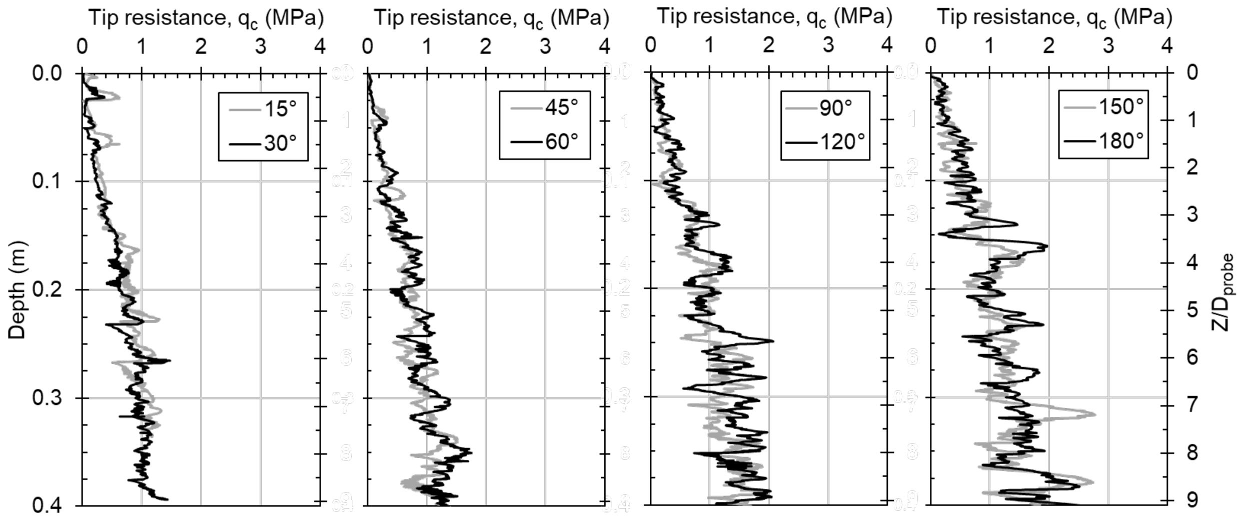

Figure 6: Depth profiles of penetration resistances measured during unconfined DEM simulations for tips with apex angles of 15°, 30°, 45°, 60°, 90°, 120°, 150°, and 180°.

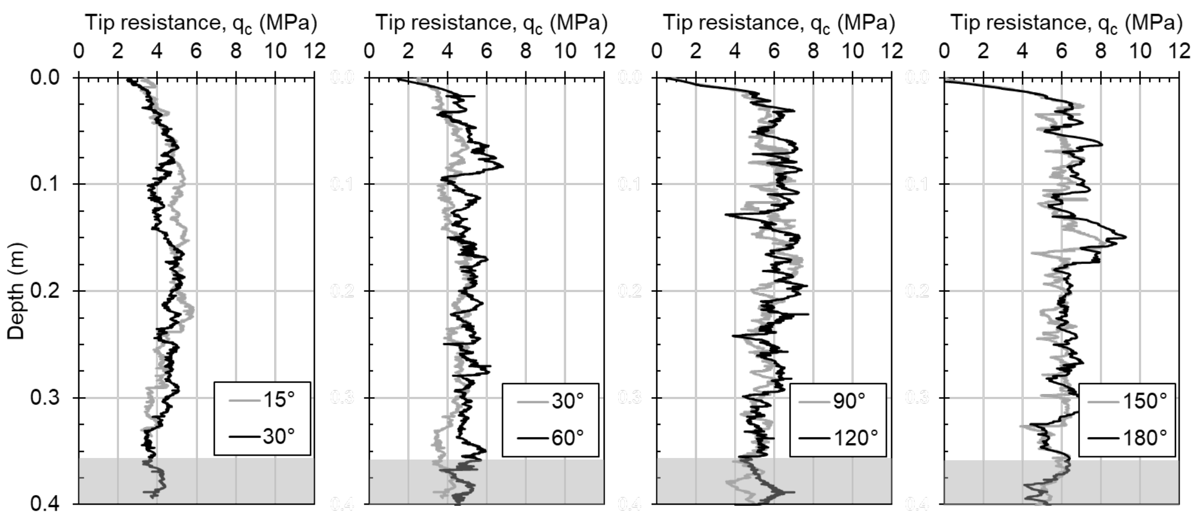

Figure 7: Depth profiles of penetration resistances measured during confined DEM simulations for tips with apex angles of 15°, 30°, 45°, 60°, 90°, 120°, 150°, and 180° (values in the shaded region are used to calculate average q_c values reported in Figure 8c).

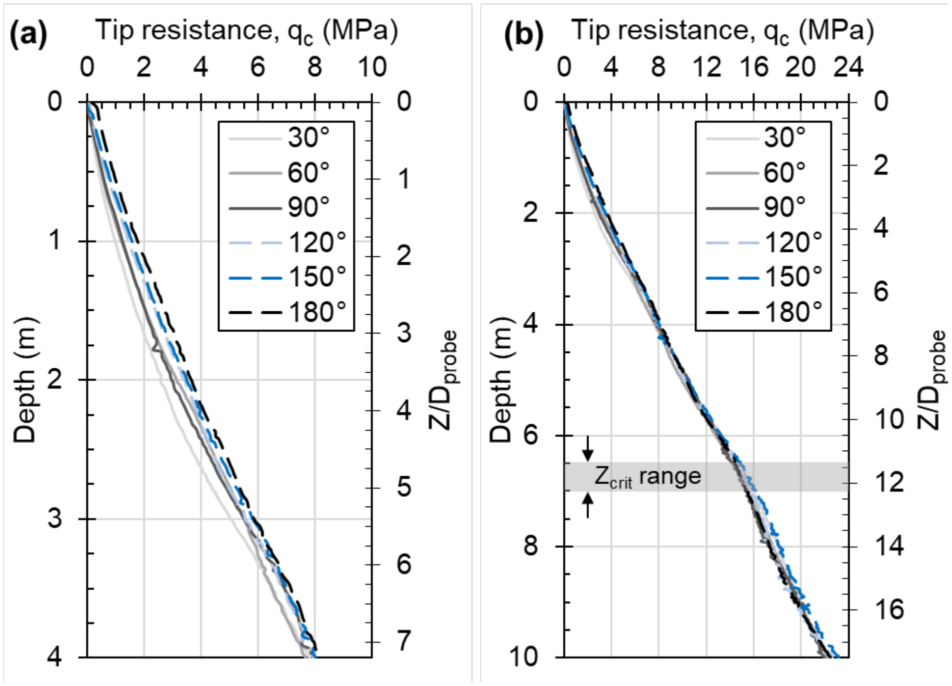

Figure 8: Depth profiles of penetration resistances measured during centrifuge penetration tests with tips of varying apex angle for (a) depth smaller than 4 m (Z/D_{probe} smaller than 7.2) and (b) entire profile.

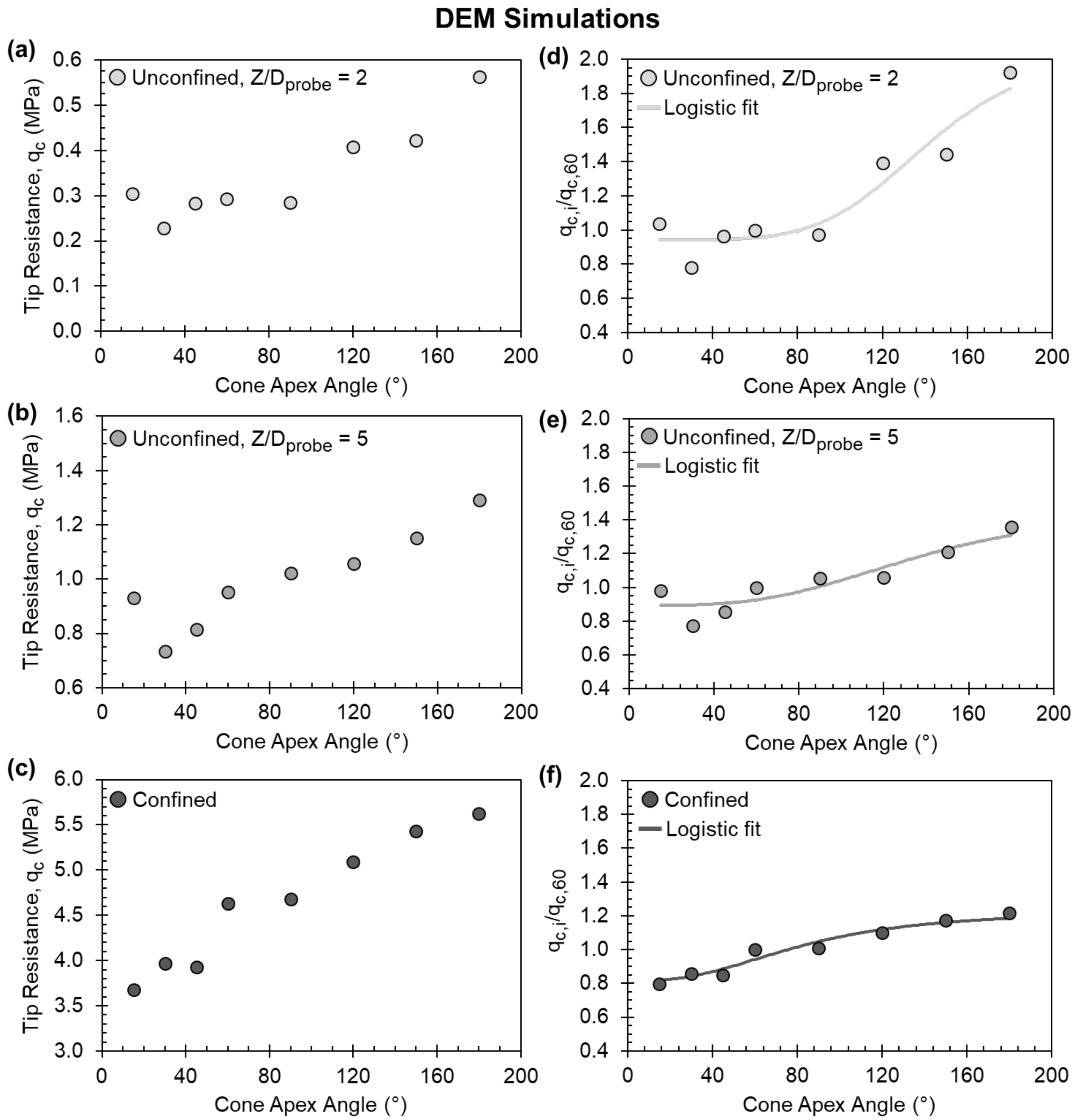

Figure 9: Absolute and normalized tip resistances measured in DEM simulations: (a) and (d) unconfined simulations at $Z/D_{probe} = 2$, (b) and (e) unconfined simulations at $Z/D_{probe} = 5$, and (c) and (f) confined simulations.

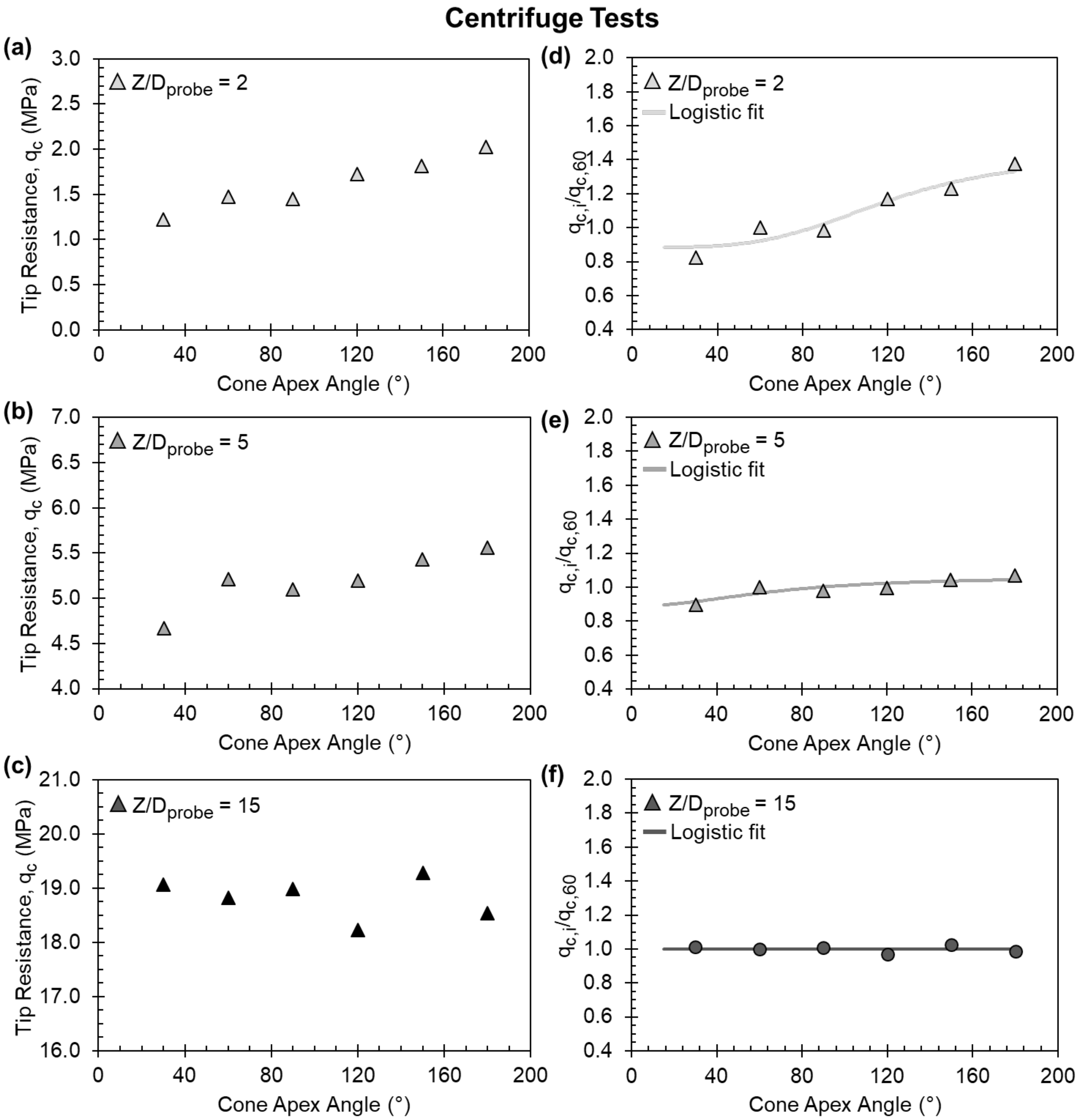

Figure 10: Absolute and normalized tip resistances measured in centrifuge penetration tests: (a) and (d) $Z/D_{probe} = 2$, (b) and (e) $Z/D_{probe} = 5$, and (c) and (f) $Z/D_{probe} = 15$.

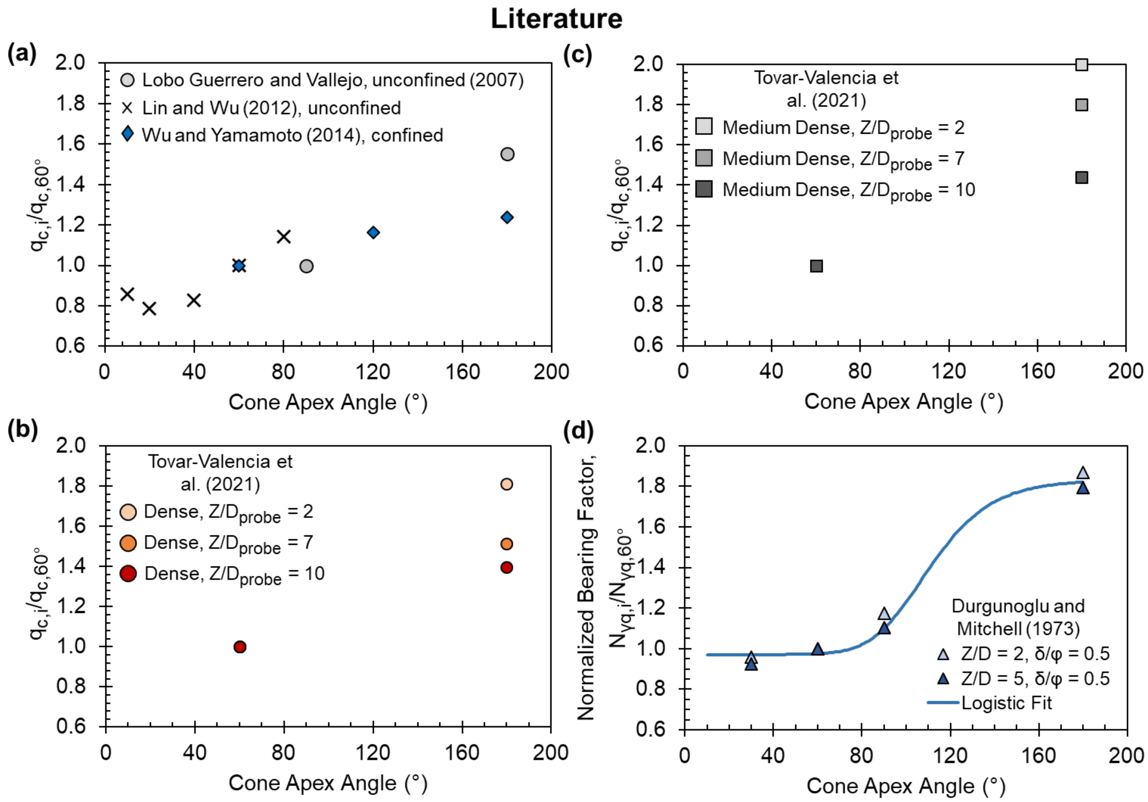

Figure 11: Normalized tip resistances from: (a) Lobo Guerrero and Vallejo (2007), Lin and Wu (2012), and Wu and Yamamoto (2014), (b) Tovar-Valencia et al. (2021) on dense sand, and (c) Tovar-Valencia et al. (2020) on medium dense sand. (d) Normalized bearing factors from Durgunoglu and Mitchell (1973) for sand with a friction angle of 36°.

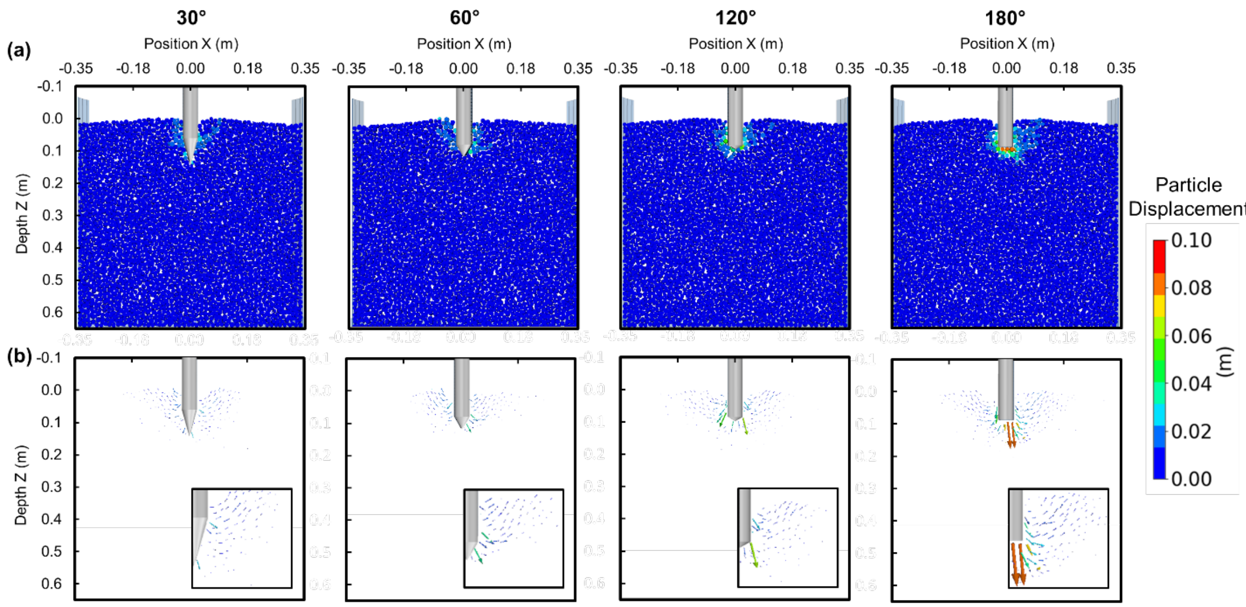

Figure 12: Particle displacements from unconfined DEM simulations with tips of varying apex angle at $Z/D_{probe} = 2$: (a) absolute particle displacements and (b) incremental particle displacement vectors.

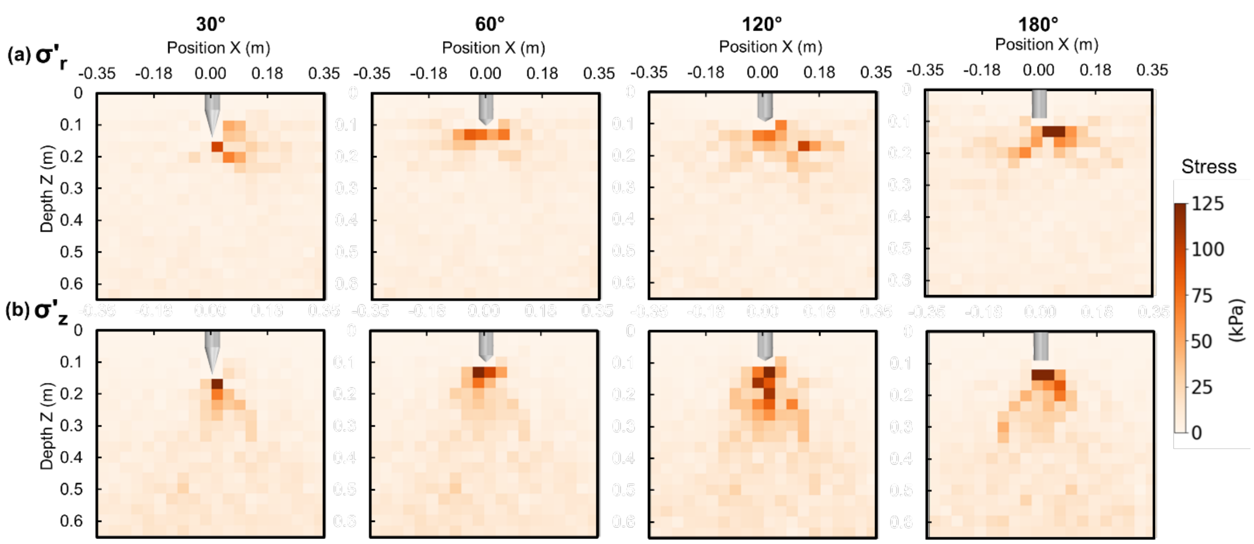

Figure 13: Effective stresses from unconfined DEM simulations with tips of varying apex angle at $Z/D_{probe} = 2$: (a) radial and (b) vertical stresses.

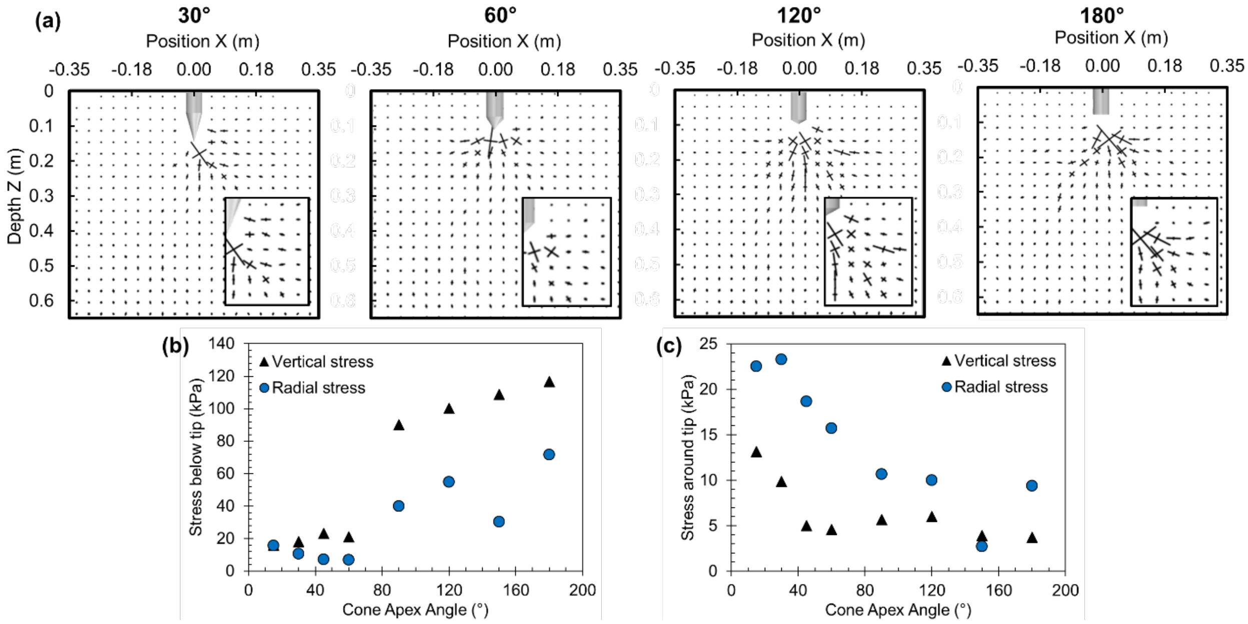

Figure 14: (a) Major and minor principal stresses from unconfined DEM simulations with tips of varying apex angle at $Z/D_{probe} = 2$. Vertical and radial stresses (b) below and (c) around the tip from unconfined DEM simulations at $Z/D_{probe} = 2$.

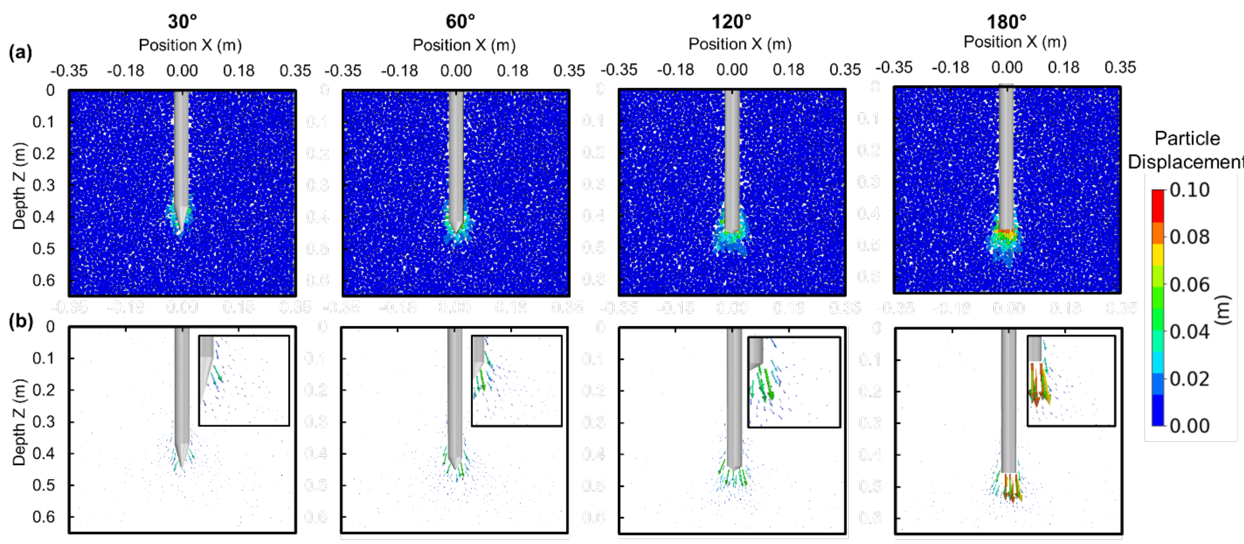

Figure 15: Particle displacements from confined DEM simulations with tips of varying apex angle: (a) absolute particle displacements and (b) incremental particle displacement vectors.

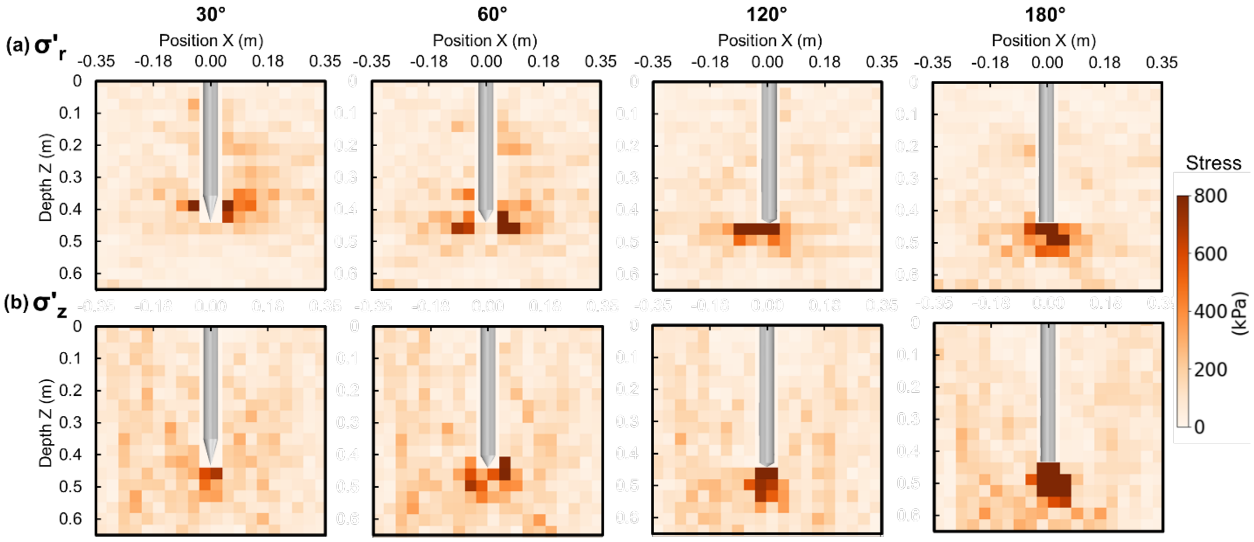

Figure 16: Effective stresses from confined DEM simulations with tips of varying apex angle: (a) radial and (b) vertical stresses.

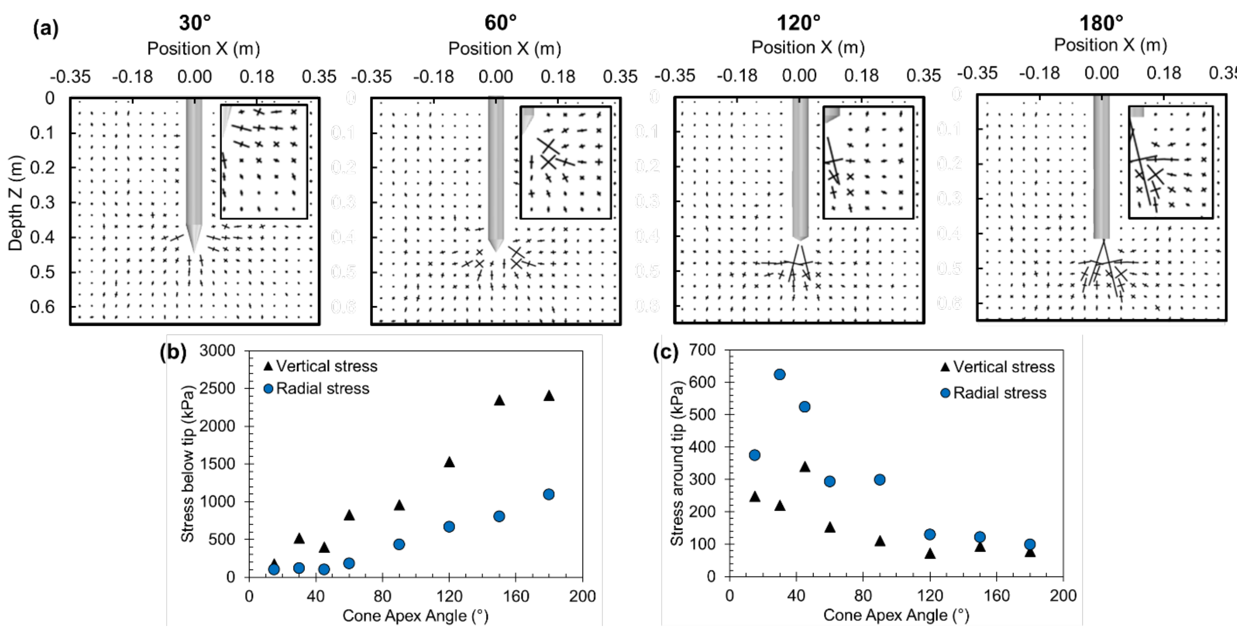

Figure 17: (a) Major and minor principal stresses from confined DEM simulations with tips of varying apex angle. Vertical and radial stresses (b) below and (c) around the tip from confined DEM simulations.

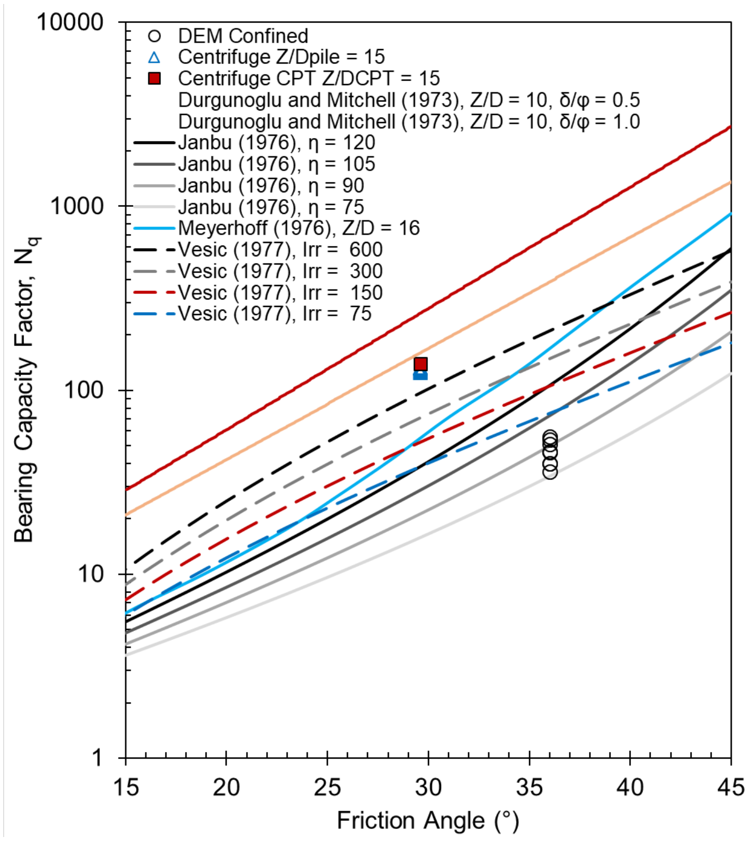

Figure S1: Comparison of bearing capacity factors from the DEM confined simulations, centrifuge tests at Z/D_{probe} of 15, and centrifuge CPT tests at Z/D_{CPT} of 15 with various analytical and semi-analytical solutions. η is the angle defining the geometry failure mechanism, Irr is the soil's rigidity index, and δ/φ is the ratio of cone-soil friction angle to soil internal friction angle. The Durgunoglu and Mitchell (1973) solution corresponds to a cone apex angle of 60°.